Gravity currents produced by constant and time varying inflow in a circular cross-section channel: experiments and theory

S. Longo[a], M. Ungarish[b], V. Di Federico[c], L. Chiapponi[a], F. Addona[a]

[a] *Dipartimento di Ingegneria Civile, Ambiente Territorio e Architettura (DICATeA), Università di Parma, Parco Area delle Scienze, 181/A, 43124 Parma, Italy*
[b] *Department of Computer Science, Technion, Israel Institute of Technology, Haifa 32000, Israel*
[c] *Dipartimento di Ingegneria Civile, Chimica, Ambientale e dei Materiali (DICAM), Università di Bologna, Viale Risorgimento, 2, 40136 Bologna, Italy*

Abstract

We investigate high-Reynolds number gravity currents (GC) in a horizontal channel of circular cross-section. We focus on GC sustained by constant or time varying inflow (volume of injected fluid $\propto\ t^{\alpha}$, with $\alpha = 1$ and $\alpha > 1$). The novelty of our work is in the type of the gravity currents: produced by influx/outflux boundary conditions, and propagation in circular (or semi-circular) channel. The objective is to elucidate the main propagation features and correlate them to the governing dimensionless parameters; to this end, we use experimental observations guided by shallow-water (SW) theoretical models. The system is of Boussinesq type with the denser fluid (salt water) injected into the ambient fluid (tap water) at one end section of a circular tube of 19 cm diameter and 605 cm long. The ambient fluid fills the channel of radius $r*$ up to a given height $H^* = \beta r^*$ $(0 < \beta < 2)$ where it is open to the atmosphere. This fluid is displaced by the intruding current and outflows either at the same or at the opposite end-side of the channel. The two different configurations (with return and no-return flow) allow to analyse the impact of the motion of the ambient fluid on the front speed of the intruding current. For Q larger than some threshold value, the current is expected theoretically to undergo a choking process which limits the speed/thickness of propagation. Two series of experiments were conducted with constant and time varying inflow. The choking effect was observed, qualitatively, in both series. The theory correctly predicts the qualitative behavior, but systematically overes-

timates the front speed of the current (consistent with previously-published data concerning rectangular and non-rectangular cross-sections), with larger discrepancies for the no-return flow case. These discrepancies are mainly due to: i) the variations of the free-surface of the ambient fluid with respect to its nominal value (the theoretical model assumes a rigid wall at the upper limit of the ambient fluid), and ii) mixing/entrainment effects, as shown by specific measurements of the open interface level and velocity profiles.

Keywords: gravity current, variable influx, experiment, shallow-water model, Froude number, choking effect

1. Introduction

The injection of a denser fluid into a lighter ambient one, or vice versa, generates a gravity current (GC), which propagates mainly in the horizontal direction. Several environmental and industrial flows are modeled according to the GC approach. Gravity currents are typically classified according to the type of release. Some large scale GCs occurring in nature, such as currents and avalanches, are characterised by a constant volume released in a relatively short time, and are thus termed lock-released GCs. Fresh water released in estuaries, hot water released from power stations into rivers and lakes, as well as lava and pyroclastic flows, are instead characterised by a constant or varying discharge on a time scale much longer than the propagation time scale of the process. The most general case is a time dependent inflow with a more or less intense initial discharge, followed by an interval with constant discharge, and ending with a progressive decrease with time.

Another factor influencing GC propagation is the shape of the cross-section. Most theoretical developments and studies refer to rectangular cross-section channels with the current propagating at the bottom or at the top; large values of Reynolds number (Re) render the lateral boundaries not relevant [1, 2]. However, many natural large-scale GCs (e.g., floods in valleys and rivers), propagate in channels with non rectangular cross-section, and industrial fluid-transport infrastructures are often designed with such cross-sections. This is so also for small scale GCs, like a cooling fluid in a drainage duct. Hence, a detailed analysis and a proper understanding of currents propagating in non-rectangular cross-sections is requested.

The lock-released GC have been analysed in details in numerous configurations, including two-dimensional and axisymmetric geometries, and several

different cross sectional shapes [e.g., 3, 4, 5, 6]. The GCs generated by constant influx [7, 8, 9] have received less attention, and the studies of the cases with time increasing (waxing) or time decreasing (waning) discharge [10, 11] are quite rare.

Many of the concepts developed for lock-released, fixed-volume GCs are relevant also for constant, waxing or waning GCs, but there are also significant differences which justify a separate dedicated analysis. The boundary conditions (location) of the outlet vs. inlet may influence the propagation of the current via the flow in the ambient (this is to some extent similar with the co- and counter-flow situations investigated by [12, 9, 13]). It is the position of the sink which makes the difference, with a return flow case, if the sink is in the same section of the inflow, and with a no-return flow case, if the sink is in the opposite section. An intermediate configuration is also allowed. These effects have been theoretically analysed in [10].

Another important aspect of the theoretical solutions of GCs, which is strongly relevant to source-sink systems, is their energetic realizability: a limit value for the front speed and for the thickness is given by the requirement of no energy gain during the propagation. This constraint is relevant when the current occupies a significant (half, say) portion of the cross-section area. Therefore, a waxing inflow current is prone to reach a 'choking' condition, if the discharge becomes larger than the choking discharge. This aspect, already discussed by [14] for inviscid GC in rectangular cross-sections, has been extended to generic cross-section currents by [15].

The motivation of the present study is to enhance the knowledge of and insights into the flow of GCs generated by sustained influx, focusing attention on a typical non-rectangular cross-section geometry. In particular, we attempt to assess the accuracy and applicability of available simple models for GC in non-rectangular cross sections, with constant or time increasing flux. Our aim is two-fold: i) to verify the effects of the flow of the ambient fluid (induced by the intruding current) on the front speed of the intruding current, and ii) to check the effectiveness of the model with respect to the choking condition. A series of experiments have been completed in a horizontal channel of circular cross-section, with salt and tap water as intruding and ambient fluid, respectively. The front speed was evaluated for all experiments, and detailed measurements of the free surface level and of the velocity profiles were conducted in some of them. There are several novelties in our work, such as: the geometry of the cross-section, the size of the channel, the fluid injection control with the possibility to reproduce a generic time varying

inflow rate function, the check of the choking effect, the two different outflow sections, the analysis (with measurements) of the ambient fluid role in the propagation of the GC, the measurements of the intruding current velocity with the estimation of the turbulence level.

The paper is organized as follows. First we introduce briefly the theoretical model (Section 2), then we describe the experimental apparatus and protocol and the experimental results (Section 3). The effects of the open interface and the velocity profiles are discussed in the next Section. Some concluding remarks are given in Section 5; then some details on the force balance and on the effects of dissipation and non uniform velocity profiles are discussed in the Appendix.

2. Theoretical model

We consider the flow of a denser current of density ρ_c in a lighter ambient fluid of density ρ_a in a horizontal channel with circular cross section of radius r^*, see Figure 1. The ambient fluid is limited by a fixed free-slip top plane at height H^*; the height/radius ratio is defined as $\beta = H^*/r^*$. We introduce the reduced gravity $g' = [(\rho_c - \rho_a)/\rho_a]g = (R-1)g$, where $R = \rho_c/\rho_a$. We scale all lengths with H^*, the depth of the ambient fluid, the velocity u^* with $U^* = (g'H^*)^{1/2}$ ($u = u^*/(g'H^*)^{1/2}$), the time t^* with H^*/U^* ($t = t^*(g'/H^*)^{1/2}$), the discharge Q^* with $H^{*2}U^*$ ($Q = Q^*/H^{*2}U^*$). The Reynolds number of the dense current, $Re = U^*H^*/\nu_c$, where ν_c is the kinematic viscosity of the dense current, is always sufficiently large to justify the assumption of an inviscid propagation. For simplicity, we discard mixing and entrainment effects. The volume of current fluid $\mathcal{V}$ is assumed of the general form $\mathcal{V} \propto t^\alpha$, with $\alpha = 0$ representing a constant volume (dam-break) process, and $\alpha = 1$ a constant inflow. The parameter γ is representative of the outflow discharge, with $\gamma = 1$ relative to the return-flow condition, and $\gamma = 0$ relative to no-return-flow condition. The problem involves numerous parameters: Re, R, β, γ, Q, α. The model used here assumes $R \approx 1$ and large Re (i.e., Boussinesq and inviscid system).

2.1. Constant inflow ($\alpha = 1$)

The results presented here are an exact solution of the two-layer shallow water equations derived in [15, 16]. For $\gamma = 1$ and constant inflow ($\alpha = 1$) the current is expected to move with constant $u = u_N$, $h = h_N$. The

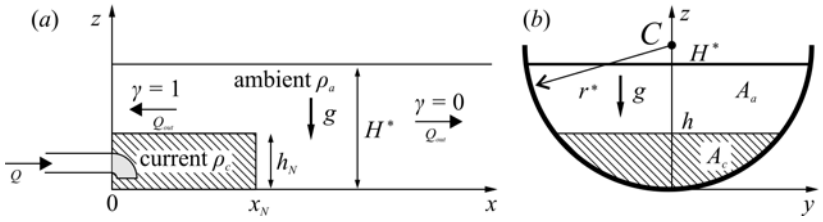

Figure 1: A schematic description of the inflow problem. The cross area of the channel is $A_T = A_c + A_a$, C is the center, r^* is the radius of the circular cross section, g is the acceleration of gravity, H^* is the ambient fluid height and h is the denser current height.

governing dimensionless balances for the current are reduced to: the volume conservation

$$Q = uA(h), \tag{1}$$

the front condition

$$u = Fr(h)h^{1/2}, \tag{2}$$

where

$$Fr^2 = \frac{2(1-\varphi)}{1+\varphi}\left[1 - \varphi + \frac{J(h)}{hA(1)}\right], \tag{3}$$

$$\varphi = A(h)/A(1). \tag{4}$$

$A(1)$ is the area occupied by the ambient fluid (in dimensionless form). For a circular cross-section with a fixed given radius, represented by $y = f(z) = (2rz - z^2)^{1/2}$ ($r = r^*/H^*$ is the dimensionless radius)

$$A(h) = \int_0^h 2(2rz - z^2)^{1/2} dz = \left[(h-r)(2rh-h^2)^{1/2} - r^2 \arcsin(1-h/r) + \frac{\pi}{2}r^2\right]; \tag{5}$$

$$J(h) = 2\int_0^h (2rz - z^2)^{1/2} z dz = -\frac{2}{3}(2rh - h^2)^{3/2} + rA(h). \tag{6}$$

Hence, it is necessary to solve the equation

$$Fr(h_N)h_N^{1/2}A(h_N) - Q = 0 \tag{7}$$

for h_N and then to calculate u_N from eq. (2). These equations for u_N and h_N are valid if the outflow of the ambient fluid and the inflow of the current

fluid are in the same section (i.e., $\gamma = 1$). In addition, we assume that the influx conditions at $x = 0$ are the appropriate u_N, h_N, or that an adjustment to these conditions occurs over a short distance (of the order of h) from the source.

A generalization of the problem includes the situation that the motion of the displaced (ambient) fluid can take place in the left end, in the right end and in both ends of the flume, with a parameter $0 \leq \gamma \leq 1$, $\gamma = 1$ indicating outflow in the same section of the inflow (previously analysed case), and $\gamma = 0$ indicating outflow in the opposite section of inflow. This last condition is also defined as 'no-return flow'. Following [10], to include the effects of the displaced ambient fluid it is necessary to solve the following equation in the unknown h:

$$\frac{1}{1-(1-\gamma)\varphi(h)} Fr(h) h^{1/2} A(h) - Q = 0, \tag{8}$$

obtaining h_N, while the front speed in the laboratory frame is equal to

$$u_N = Fr(h_N) h_N^{1/2} + (1-\gamma)\frac{Q}{A(1)}. \tag{9}$$

2.2. Flow in choking condition and variable inflow

The choking condition is defined as the limiting condition corresponding to no dissipation, and is computed by solving the following equation, based on the energy criterion by Benjamin-Ungarish (see [15]):

$$Fr^2(h_N) = 2(1-\varphi(h_N))^2. \tag{10}$$

Figure 2 shows the value of the discharge in choking conditions for the two cases of sink in the same ($\gamma = 1$) or in the opposite ($\gamma = 0$) section with respect to the source. The latter case gives values always larger than the former. Recall that $\beta = 2$ means that the height of the fluids fills the entire tube section diameter. We see that in this (or close) circumstance, choking occurs at relatively small influx. As the height H^* increases (keeping the same tube radius r^*), a larger Q is possible before choking is attained. Some of our experiments were designed close to and within the theoretically predicted chocking conditions, to provide some qualitative and quantitative confirmations of this theoretical prediction.

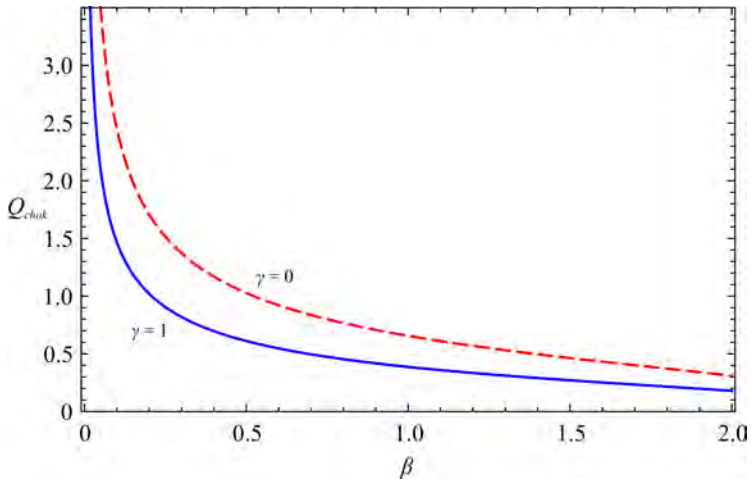

Figure 2: The values of the theoretical threshold discharge for choking conditions as a function of β for $\gamma = 1$ (return flow, blue continuous curve) and for $\gamma = 0$ (no-return flow, dashed red curve).

The experiments with time-dependent influx $Q(t)$ conditions have been compared with box-model estimates. The box-model is based on the assumption that the height of the current is uniform in x, with $h(x) = h_N$ for $0 \leq x \leq x_N$, hence only mass conservation in integral form is necessary:

$$x_N(t) = \frac{\mathcal{V}(t)}{A(h(t))}, \tag{11}$$

(in dimensionless form), with the front-end condition represented by eq. (9), $\mathcal{V}$ representing the volume of injected fluid, and $u_N = dx_N/dt$.

Substituting eq. (11) into eq. (9) yields the following ODE

$$\frac{dh}{dt} = -\frac{A^2(h)}{\mathcal{V}(t) f(h)} \left[Fr(h) h^{1/2} + (1-\gamma) \frac{Q(t)}{A(1)} - \frac{Q(t)}{A(h)} \right]. \tag{12}$$

The numerical integration of eq. (12) with the initial condition $h(0) = 0$ gives $h(t)$ and $x_N(t)$. For constant influx ($\alpha = 1$), the solutions of the SW equations and of the box-model coincide: eq. (12) admits the solution $h = h_N = \text{const.}$ and eq. (2) is recovered. The main advantage of the models presented in this section is their mathematical simplicity: the highly relevant properties of propagation speed, thickness, presence/absence of choking, and effect of the position of the outflux (sink) are predicted by simple equations

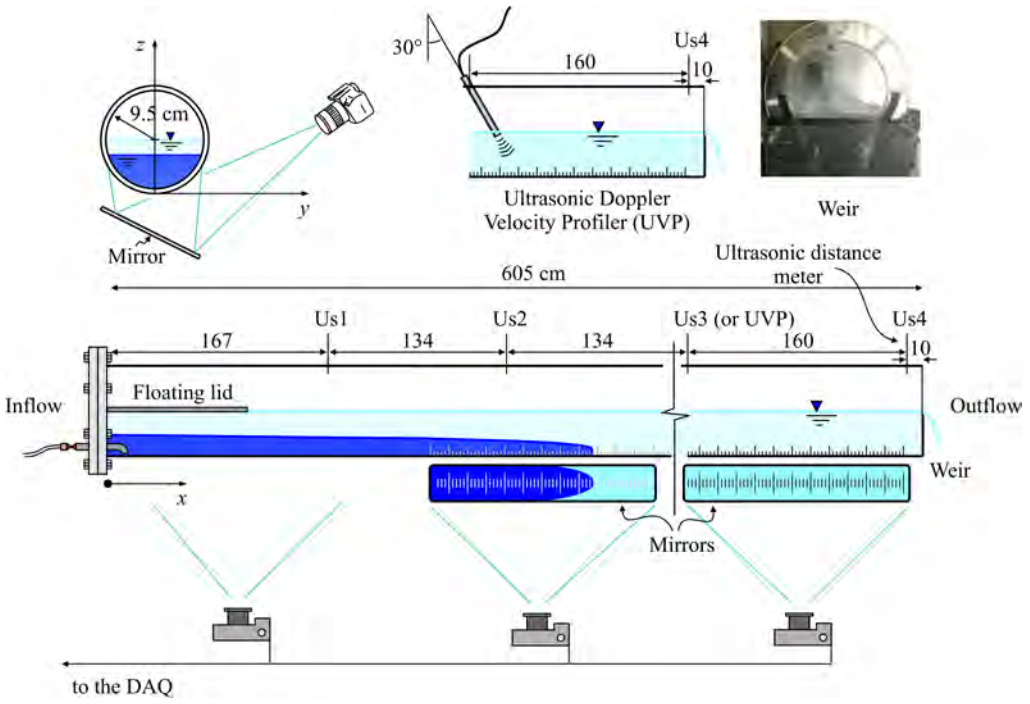

Figure 3: Schematic description of the experimental apparatus.

whose solution can be obtained rather immediately on a laptop computer. As such, they provide valuable guiding lines and estimates for applications. On the other hand, in view of the approximate nature of these simple results, it is necessary to use experiment for a more comprehensive understanding of the flow field and also for assessing the accuracy of the theoretical predictions.

3. The experiments

3.1. The experimental apparatus

The experimental apparatus was a circular tube of transparent thermoplastic, with internal radius $r^* = 9.5\,\text{cm}$ and a length of 605 cm (see also [3] for more details). At the inflow section, a pipe with axis of the exit section orthogonal or parallel to the bottom of the tube was connected to a centrifugal pump controlled by an inverter. The flow rate was measured by a turbine meter with an overall accuracy equal to 1% of the instantaneous value. The turbine meter was the sensor of a Proportional-Integral-Derivative (PID) feedback control system to guarantee the desired value of discharge.

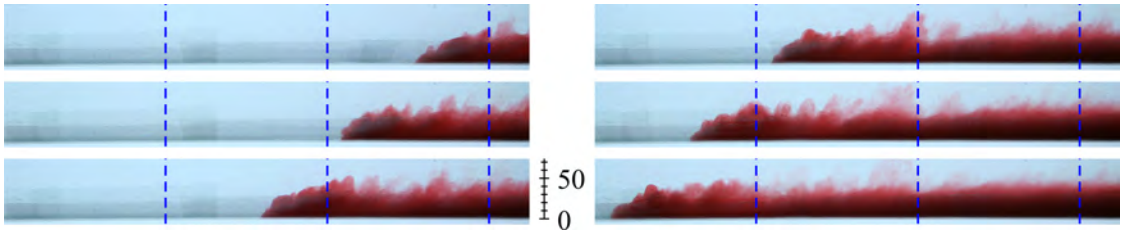

Figure 4: Photographs showing profiles of the head of the GC, side view, in Experiment 12, $Re = 20.6 \times 10^3$, $\gamma = 0$. The vertical dashed lines are 20 cm apart and the times since release are 24, 25, 26, 27, 28, and 29 s.

In the outflow section there was a weir with horizontal crest, to maintain a constant level of the interface between the ambient fluid and air during the experiments (as we will discuss later, the level of the interface is subjected to fluctuations and to a significant growth during the advancement of the denser current). The level of the crest was adjusted to fix different values of H^*.

The front position of the currents was measured by four photo cameras (Canon EOS 2D and 3D, 3456×2304 pixels, 4368×2912 pixels, respectively) with a data rate of 1 frame per second (f.p.s.) in a fixed position, and by a full HD video camera (Canon Legria HF 20, 1920x1080 pixels) with data rate of 25 f.p.s. in a fixed position or moved parallel to the pipe in order to get the nose of the current in the Field of View (FOV). The size of the FOV of each photo camera was varying from ≈ 100 cm to ≈ 150 cm, with a spatial resolution of ≈ 25 pixels/cm. A grid was stuck at the bottom of the tube, and was used for detecting the coordinates of the points used for the planar restitution of the images in the FOV. The overall uncertainty in image data processing was less than 0.2 cm for the measured front position. A typical sequence of images for Experiment 12 is shown in Figure 4. For a limited number of experiments the ambient fluid free surface level was measured by four Ultrasonic distance meters (Us1, Us2, Us3 and Us4 in Figure 3) (Turck Banner Q45UR) with an accuracy of 0.03 cm and a time response of 10 ms. Details on the accuracy of this instruments are discussed in [17], [18].

For some experiments the velocity of the dense fluid current was measured in the mid-vertical section by an Ultrasound Velocity Profiler (UVP, model DOP 2000 Signal-Processing S.A., Switzerland, 2005) installed at an angle of $\approx 30^\circ$ at $x = 1650$ cm from one end of the channel, by using the same access generally used for the Ultrasonic distance meter Us3. In the adopted

configuration the probe acquires the velocity in 96 volumes of measurements with a spatial resolution of 0.12 cm (along the axis of the probe) and with a data rate of $\approx$ 44 Hz (number of profiles acquired per second). See [17] for more details on the instrument and on its applications.

3.2. The uncertainty in measurements and in parameters

Here we estimate the experimental uncertainties affecting problem parameters; the analysis includes both systematic and random uncertainties. The mass density of the ambient fluid (tap water) and of the dense fluid (salt added water plus aniline) were measured by a pycnometer with an uncertainty of 10^{-3} g cm^{-3}. The corresponding uncertainty for the parameter $R = \rho_c/\rho_a$ is $\Delta R/R = 0.2\,\%$. The same uncertainty holds for the reduced gravity g'. The level of the ambient fluid was detected with an accuracy of 0.1 cm (except for measurements taken with the Ultrasonic distance meters), inducing a relative uncertainty $\Delta H^*/H^* \leq 2\,\%$ and $\Delta\beta/\beta \leq 3\,\%$ by assuming that the radius of the channel had an absolute uncertainty of 0.1 cm. The velocity scale had an uncertainty $\Delta U^*/U^* \leq 1.1\,\%$ and the time scale had an uncertainty equal to $\Delta T^*/T^* = 3.1\,\%$. The discharge was measured with uncertainty equal to 1 % of the instantaneous value and the dimensionless discharge had an uncertainty equal to $\Delta Q/Q = 6.1\,\%$. By assuming an uncertainty of 1 % in the value of the kinematic viscosity of the dense fluid, the Reynolds number had an uncertainty equal to $\Delta Re/Re \leq 4.1\,\%$.

The front position was detected with an absolute uncertainty of 0.3 cm at a time affected by an uncertainty equal to $0.5/25 = 0.02$ s for the video frames, and equal to 0.07 s for the photo cameras. The front speed was computed by fitting a line to the experimental time series of front position with the maximum likelihood method, and by computing the uncertainty of the parameter of the line inclination (i.e., the front speed), with a maximum expected value equal to $\approx$ 0.3 cm s^{-1}. Since the minimum front speed in the present set of experiments is equal to 4.8 cm s^{-1}, it results that the dimensional front speed had uncertainty $\leq 6.3\,\%$ and its dimensionless counterpart is $\Delta u_N/u_N \leq 7.3\,\%$. The uncertainty of the dimensional front position at $x_N = 100$ cm is $\leq 0.3\,\%$, its dimensionless counterpart is equal to $\Delta x_N/x_N \leq 2.3\,\%$ and has asymptotical value $\Delta x_N/x_N \leq 2\,\%$ when the front of the current reaches the end of the channel. The free surface level measured by the Ultrasonic distance meters was affected by an uncertainty of 0.03 cm and the space gradient between the most distant sensors had an absolute uncertainty equal to $\approx 9 \times 10^{-5}$. The velocity measured by the UVP had

an uncertainty of 4 % of the measured value, with a minimum of 0.3 $\mathrm{cm\,s^{-1}}$. An absolute uncertainty of 0.1 cm was associated with the vertical position where the measurement of the horizontal velocity is made.

3.3. The experimental results

A series of experiments have been carried out in order to measure the speed of the front of gravity currents propagating in a horizontal channel of circular cross-section. The injected fluid was salt water with density in the range $1020 - 1117\,\mathrm{kgm^{-3}}$, added with aniline dye to facilitate the image analysis, the ambient fluid was tap water. The density ratios $R - 1 = (\rho_c - \rho_a)/\rho_a$ were in the range $2.1 - 11.8\%$. The injected volume of dense fluid is $\mathcal{V}(t) \propto t^\alpha$ and the corresponding flux, proportional to $\alpha t^{\alpha-1}$, is constant ($\alpha = 1$) or time increasing ($\alpha > 1$). The parameters for the two cases $\alpha = 1$ and $\alpha > 1$ are listed in Table 1 and in Table 2, respectively. In some experiments the value of Q is larger than the threshold Q_{chok} (see Figure 2) and hence the current is expected to be in choking conditions. Some experiments were repeated in order to check the short and long term reproducibility.

Figure 5 shows the theoretical and the experimental front speed against the inflow rate. Front speed u_N increases with Q for both no-return (Figure 5*a*) and return (Figure 5*b*) conditions. In the case of latter, a plateau is reached, interpreted as flow under choking conditions. In the case of no-return flows there is no evidence of choking conditions in our experimental data (Figure 5*a*). The calculated height of the current, h_N, is around 0.5 in the tested cases. This is consistent with the observations; we do not show comparisons for h_N because it is not a clear-cut experimental variable.

Figure 6 shows the relative difference between the measured and theoretical front speed. The agreement between theory and experiments is generally better for the 'return' condition ($\gamma = 1$) and for constant inflow ($\alpha = 1$), especially if the flow is choked. It seems that higher Reynolds number experiments are prone to give results with larger discrepancies with theory. In choking conditions, the disturbances of the free-surface and the interferences between counterflowing currents were more relevant with respect to most experiments in no-choking conditions (see §4). In fact, to reproduce the choking conditions it was necessary to use a high discharge of a low density current advancing in an ambient fluid of limited depth. All these prescriptions facilitate the jet-like behavior of the current at the inflow section, with

Exp.	$R-1$ (%)	β	H^* (cm)	g' ($\mathrm{cm\,s^{-2}}$)	Re ($\times 10^3$)	Q	U^* (cm/s)	T^* (s)	γ	
38	4.1	0.51	4.8	40	5.8	1.22	14	0.35	0	c
40	4.1	0.51	4.8	40	5.8	1.43	14	0.35	1	c
39	4.1	0.51	4.8	40	5.8	1.69	14	0.35	0	c
41	4.1	0.51	4.8	40	5.8	2.04	14	0.35	1	c
36	2.1	0.63	6.0	21	5.9	0.71	11	0.54	0	
37	2.1	0.63	6.0	21	5.9	1.00	11	0.54	0	c
42	6.9	0.63	6.0	68	9.8	0.91	20	0.30	1	c
43	11.8	0.63	6.0	116	11.7	0.57	26	0.23	1	c
44	11.8	0.63	6.0	116	11.7	0.70	26	0.23	1	c
45	11.8	0.63	6.0	116	11.7	0.67	26	0.23	1	c
19	2.1	1	9.5	21	11.7	0.07	14	0.68	1	
16	2.1	1	9.5	21	11.7	0.08	14	0.68	1	
17	2.1	1	9.5	21	11.7	0.13	14	0.68	1	
18	2.1	1	9.5	21	11.7	0.21	14	0.68	1	
15	2.1	1	9.5	21	11.7	0.34	14	0.68	0	
2	4.0	1	9.5	39	15.8	0.12	19	0.49	0	
28	4.1	1	9.5	40	16.0	0.05	20	0.49	1	
1	4.1	1	9.5	40	16.0	0.07	20	0.49	0	
27	4.1	1	9.5	40	16.0	0.09	20	0.49	1	
26	4.1	1	9.5	40	16.0	0.16	20	0.49	1	
14	4.6	1	9.5	45	17.0	0.23	21	0.46	0	
5	6.8	1	9.5	67	19.3	0.07	25	0.38	0	
25	6.9	1	9.5	68	19.4	0.04	25	0.37	1	
33	6.9	1	9.5	68	19.4	0.04	25	0.37	1	
23	6.9	1	9.5	68	19.4	0.07	25	0.37	1	
24	6.9	1	9.5	68	19.4	0.12	25	0.37	1	
13	6.9	1	9.5	68	19.4	0.19	25	0.37	0	
3	8.1	1	9.5	80	20.4	0.05	27	0.35	0	
34	8.1	1	9.5	80	20.4	0.05	27	0.35	0	
20	8.1	1	9.5	80	20.4	0.05	27	0.35	1	
22	8.1	1	9.5	80	20.4	0.07	27	0.35	1	
4	8.2	1	9.5	80	20.4	0.09	28	0.34	0	
21	8.1	1	9.5	80	20.4	0.08	27	0.35	1	

(continue)

Exp.	$R-1$ (%)	β	H^* (cm)	g' ($\mathrm{cm\,s^{-2}}$)	Re ($\times 10^3$)	Q	U^* (cm/s)	T^* (s)	γ
12	8.3	1	9.5	81	20.6	0.17	28	0.34	0
7	11.8	1	9.5	116	23.3	0.04	33	0.29	0
29	11.8	1	9.5	116	23.3	0.03	33	0.29	1
31	11.8	1	9.5	116	23.3	0.05	33	0.29	1
8	11.8	1	9.5	116	23.3	0.05	33	0.29	0
9	11.8	1	9.5	116	23.3	0.05	33	0.29	0
6	11.8	1	9.5	116	23.3	0.07	33	0.29	0
10	11.8	1	9.5	116	23.3	0.09	33	0.29	0
35	11.8	1	9.5	116	23.3	0.09	33	0.29	0
30	11.8	1	9.5	116	23.3	0.14	33	0.29	1
32	11.8	1	9.5	116	23.3	0.13	33	0.29	1
11	11.8	1	9.5	116	23.3	0.14	33	0.29	0
(continued)									

Table 1: Parameters of the experiments with constant flux. The internal radius of the cross section is $r^* = 9.5\,\mathrm{cm}$, the length of the channel is 605 cm. $g' = [(\rho_c - \rho_a)/\rho_a]g$ is the reduced gravity, $Re = U^*H^*/\nu_c$ is the Reynolds number with ν_c the kinematic viscosity of the denser fluid varying in the range $1.136 \times 10^{-2} - 1.353 \times 10^{-2}\,\mathrm{cm^2 s^{-1}}$, $U^* = \sqrt{g'H^*}$ and $T^* = H^*/U^*$ are the velocity and the time scale, respectively. Q is the non dimensional discharge with respect to $H^{*2}U^*$. $\gamma = 0, 1$ indicates that the outflow is in the opposite/same section of the inflow. The letter 'c' in the last column indicates that the flow is in the theoretically-predicted choking conditions i.e., $Q/Q_{chok} > 1$.

Exp.	$R-1$ (%)	β	H^* (cm)	g' (cm s^{-2})	Re ($\times 10^3$)	$Q_{min-max}$	α	U^* (cm/s)	T^* (s)	γ	
46	6.9	0.56	5.3	68	8.1	0.00 - 1.16	2	18.9	0.28	1	c
47	6.3	1.00	9.5	62	18.6	0.00 - 0.31	2.64	24.2	0.39	0	
51	2.2	0.74	7	22	7.6	0.17 - 1.00	2	12.3	0.57	0	c
57	4.2	0.53	5	41	6.2	0.12 - 1.45	2	14.4	0.35	0	c
50	4.1	0.74	7	40	10.1	0.10 - 0.73	2	16.8	0.42	0	
48	6.9	0.74	7	68	12.3	0.10 - 0.56	2	21.8	0.32	0	
49	6.9	0.74	7	68	12.3	0.08 - 0.56	2	21.8	0.32	0	
52	11.3	0.74	7	111	14.4	0.40 - 0.44	2	27.9	0.25	0	
56	2.1	0.53	5	21	4.5	0.29 - 2.36	2	10.2	0.49	0	c
55	4.1	0.53	5	40	6.1	0.22 - 1.69	2	14.2	0.35	0	c
54	6.9	0.53	5	68	7.4	0.18 - 1.30	2	18.4	0.27	0	c
53	11.3	0.53	5	111	8.7	0.18 - 1.02	2	23.5	0.21	0	c
58	4.2	0.52	4.9	41	6.0	0.29 - 1.52	2	14.2	0.34	0	c
59	4.2	0.52	4.9	41	6.0	0.29 - 1.70	2	14.2	0.34	0	c
60	4.2	0.52	4.9	41	6.0	0.29 - 1.70	2	14.2	0.34	0	c

Table 2: Parameters of the experiments with variable flux. For caption see Table 1.

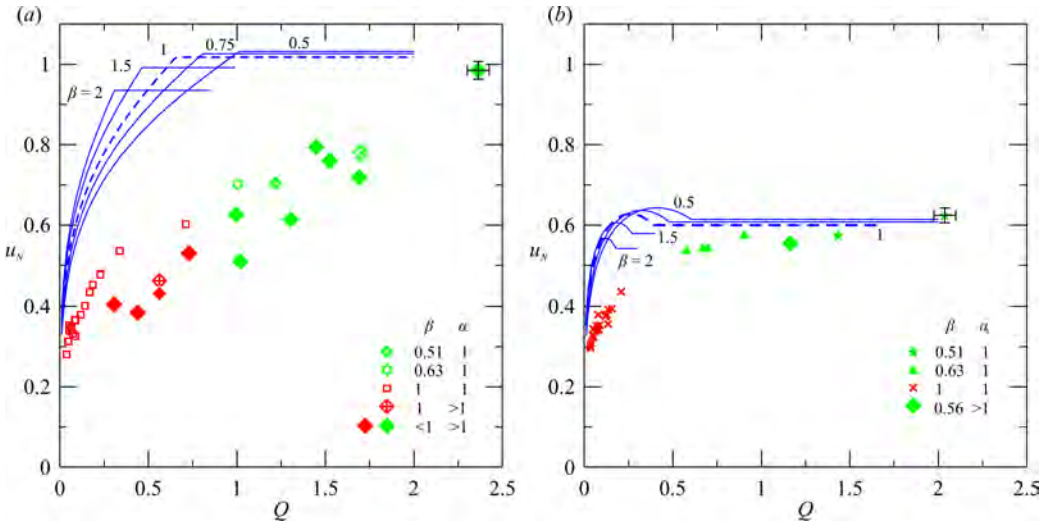

Figure 5: Comparison between theoretical and experimental front speed: (a) data for $\gamma = 0$ (no-return flow); (b) data for $\gamma = 1$ (return flow). The empty symbols and crosses refer to constant inflow experiments ($\alpha = 1$), the filled symbols refer to time varying inflow experiments ($\alpha > 1$). Red and green colors indicate the theoretically-predicted no-choking and choking conditions, respectively. The curves refer to the theoretical values for $\beta = 1$ (dashed curve) and for $\beta = 2, 1.5, 0.75, 0.5$ (continuous curves). The error bars refer to a single value of the uncertainty.

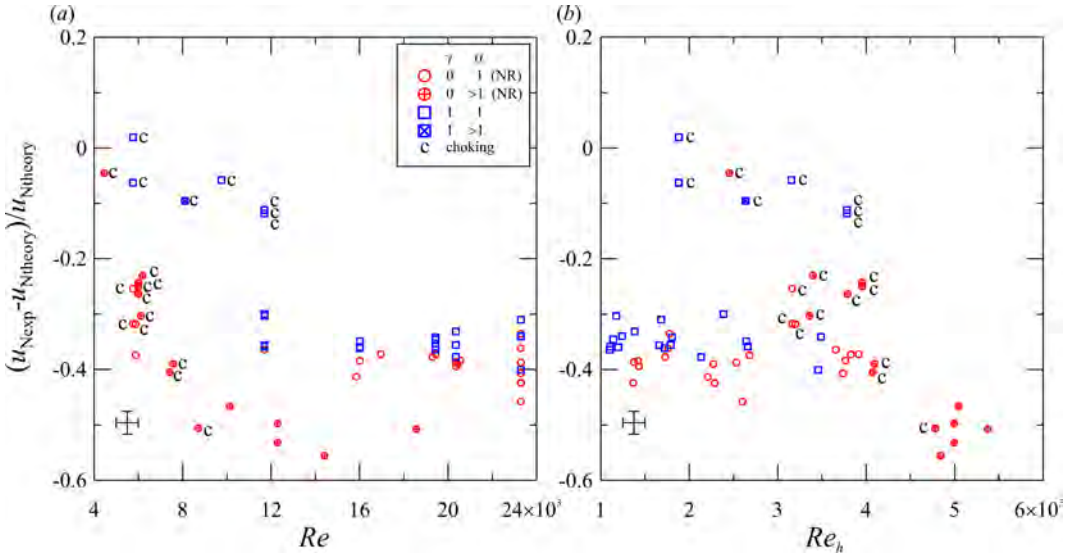

Figure 6: The relative error in predicting the speed of the front as a function of the Reynolds number. (a) Reynolds number referred to the geometry of the ambient fluid, computed as $Re = U^*H^*/\nu_c$; (b) Reynolds number referred to the geometry of the current, computed as $Re_h = h_N^* u_N^*/\nu_c$. Red circles refer to no-return flow cases, blue boxes refer to return flow cases, the letter 'c' near the symbol indicates that the experiment is in theoretically-predicted choking conditions. The error bars refer to a single value of the uncertainty.

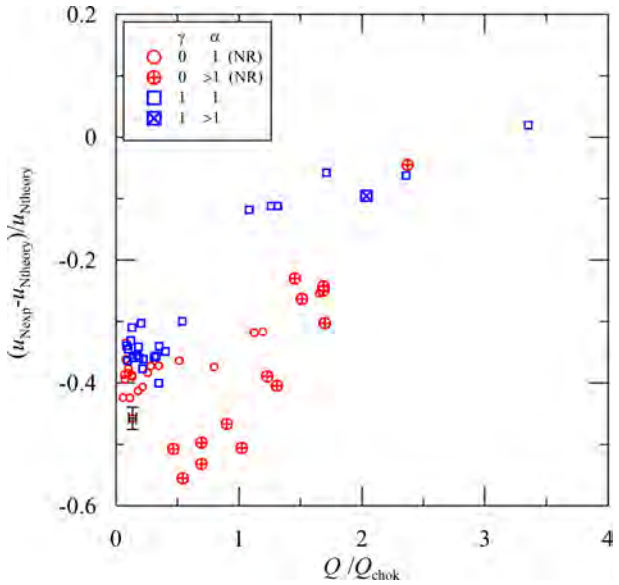

Figure 7: The relative error in predicting the front speed as a function of the relative discharge with respect to the dimensionless parameter Q/Q_{chok}. The error bars refer to a single value of the uncertainty.

consequent large disturbances of the free surface (interface between the ambient fluid and the air). A lid of length 80 cm set up near the source was effective in damping most of the fluctuations of the free surface of the ambient fluid. The lid was also effective in preventing interferences between counterflowing currents, separating the dense current from the light ambient fluid if the 'return' flow setup was tested. Without lid, there was a short circuit of the inflow current, which was washed out by the outflow; for this reason only one experiment with very large inflow discharge, Exp. #46, was performed in 'return' condition. The no-return flow experiments show large deviations with respect to theoretical estimates, in particular for cases with $\alpha > 1$. We first postulate that the channel is not long enough to allow stationarity of the current if the discharge is itself increasing in time. A more detailed explanation of the discrepancies shall be given in the analysis of the level of the free surface (see §4.1 and §4.2).

Figure 7 shows data similar to Figure 6 but the relative differences between experimental and theoretical front speed is plotted against the ratio between inflow discharge Q in the appropriate experiment and that corresponding to theoretical threshold choking conditions, Q_{chok}. For most ex-

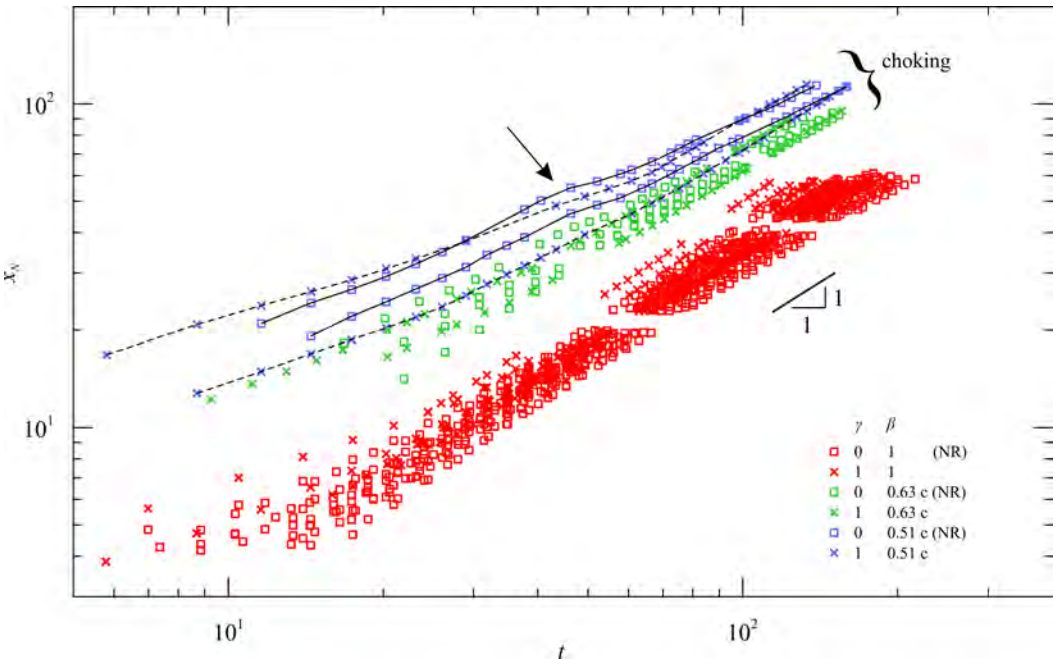

Figure 8: The distance of propagation of the currents measured from the source for experiments with constant inflow. The letter 'c' indicates a choking condition, NR stands for No-Return flow. The arrow indicates a deceleration of the current. The continuous curves refer to experiments in choking condition and no-return flow, the dashed curves to experiments in choking condition and return flow. The parameters of the experiments are listed in Table 1.

periments, the theory overestimates the measured speed by up to 40%; the overestimation sharply decreases in 'return' flow experiments in choking conditions ($Q/Q_{chok} > 1$); the agreement with theory is better for very large values of Q/Q_{chok}. The 'no-return' flow experiments show a similar trend, with an agreement with theory increasing for increasing relative discharge. For these experiments, the comparison refers to the final conditions, i.e., after the attainment of constant influx and constant front speed.

Figure 8 shows the dimensionless data plotted together for all of the experiments with $\alpha = 1$ (constant inflow) in a loglog plot (one experimental point out of five is drawn for a clear visualization). Two groups are evident, one relative to no-choking tests, the second relative to choking tests. The advancement reaches stationarity at short distance from the source for no-

choking experiments, with uniform front speed (linear curve in the diagram). The evolution is more complex for choking tests. The continuous curves refer to two experiments in no-return flow: at the beginning the current advances with increasing speed, then decelerates (see the arrow) and then again moves at a constant speed. A similar behavior, albeit much less evident, is typical of currents in choking conditions with return flow, see the dashed curves. We can infer that the deceleration starts at the first appearance of choking effects, which prevent the flow discharge to be larger than the maximum value Q_{chok} in sections beyond the critical section and induce a back flow. The scenario is similar for the return flow cases, but the back flow of the dense current is limited due to the occurrence of a current of ambient fluid toward the source. The overall effect of the return flow is a smooth transition to choking conditions. In passing, for the return flow case the theory predicts the deceleration of the current after reaching a maximum value and before entering in choking conditions, see panel (b) in Figure 5.

Figure 9 refers to experiments with time varying inflow ($\alpha > 1$) obtained in most cases with a linear ramp of the flow discharge ($\alpha = 2$) which starts at the end of a constant inflow (in most cases equal to 100 ml/s for 30 s), reaches its final maximum value and then remains constant. Only Exp. #47, #57 and #58 differ, since Exp. #47 has discharge $\propto t^{1.64}$ ($\alpha = 2.64$), Exp. #57 and Exp. #58 have a linear increasing discharge ($\propto t$, $\alpha = 2$) but with a fast ramp starting a few seconds after the start of the injection. All experiments are in no-return flow cases except for Exp. #46, and most experiments reach the theoretically-predicted choking conditions.

Figure 10a shows the front position for Exp. #47 with the discharge increasing over time as $t^{1.64}$ ($\alpha = 2.64$). The experimental front position varies $\propto t^{1.25}$, with the value of the exponent 11% smaller than the theoretical value $\delta_I = (2\alpha+3)/4 = 1.41$; see Appendix B for the details on computations.

Figure 10b shows the details of the discharge and of the front position for Exp. #56. The initial constant discharge generates a current advancing with a constant speed $u_N = 49\,\mathrm{cm\,s^{-1}}$. The increasing discharge reaches the theoretical value Q_{chok} at time t_{1chok}, generates an acceleration of the current which again recovers a uniform motion at constant front speed $u_{Nchok} = 100\,\mathrm{cm\,s^{-1}}$ a few seconds later, at time t_{2chok}. This experiment is similar to experiments performed by [11] with sudden flow-rate changes in a rectangular channels. He found that in some conditions a sequence of solitary waves develop at the interface and transfer the information to the front of the current. In other conditions, as for the case of a smooth flow-rate change,

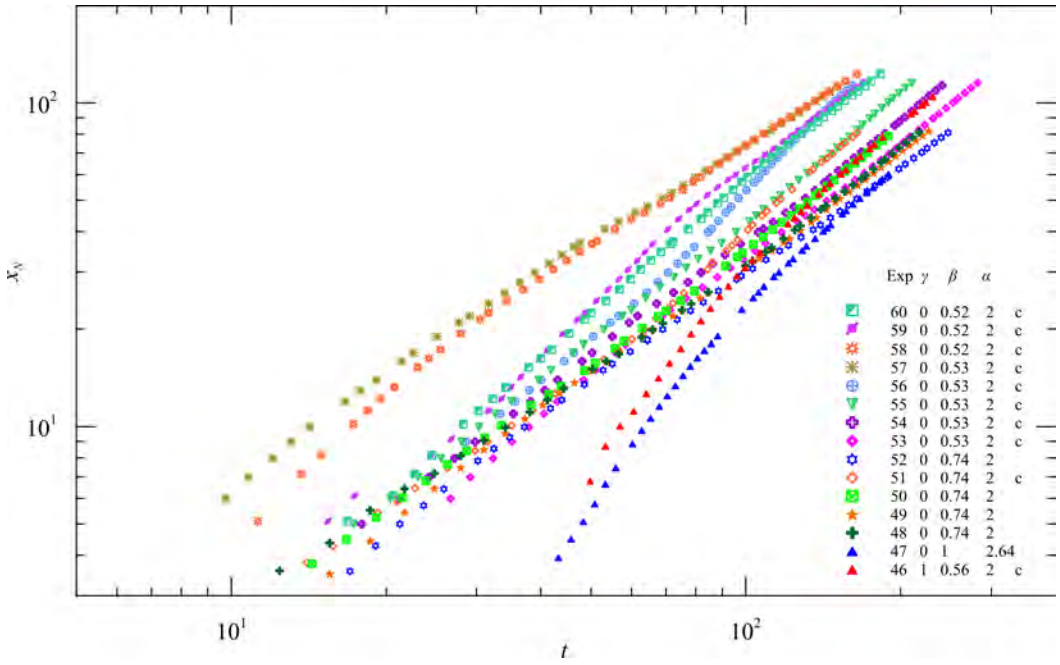

Figure 9: The distance of propagation of the current measured from the source for experiments with time increasing inflow. The discharge has a ramp shape except for Exp. #47, #57 and #58 (note the initial plateau of the discharge followed by a linear increase, see Figure 10). For clarity, only one point out of five is plotted. The letter 'c' indicates a choking condition. The parameters of the experiments are listed in Table 2.

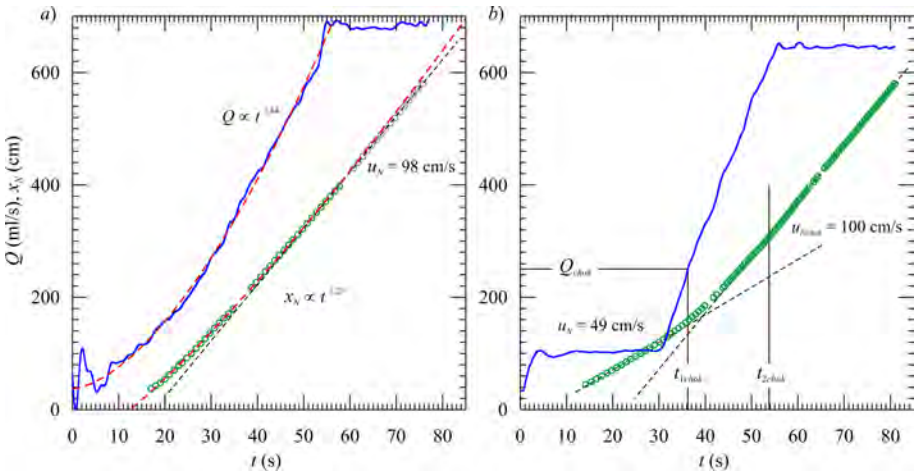

Figure 10: The distance of propagation of the current versus time for: *a*) Experiment #47 with discharge (continuous curve) $Q \propto t^{1.64}$, $\alpha = 2.64$. *b*) Experiment #56 with discharge varying following a linear ramp. The discharge (continuous curve) shows an initial plateau, a ramp ($Q \propto t$, $\alpha = 2$) and a final plateau. The dashed curves are the polynomial curve fits.

it seems plausible that the information is transferred by kinematic waves traveling faster than solitary waves.

4. Influence of the conditions at the top boundary

4.1. The free surface evolution

In the theoretical models the ambient fluid is assumed to be confined by a rigid free-slip plane at the top. However, in the experimental system the top is mostly an open surface. If the current occupies a small fraction of the channel cross section, the flow in the ambient is weak, and the exact conditions for the ambient fluid at the side boundaries and at the top boundary are unimportant. In our experiments the current occupies about half of the height of the two-fluid system, and hence the motion of the ambient fluid, and the conditions at the side and top boundaries, may affect the flow of the current. First, if the sink (discharge point of ambient fluid) is at the same end of the channel as the source, the current front encounters an ambient fluid at rest and the ambient fluid occupying the upper part of the section invaded by the dense fluid flows in the opposite direction of the current; if the sink at in the opposite end of the channel with respect to the source, the ambient

fluid beyond the front is advancing in the same direction of the current, while the residual ambient fluid is at rest. Second, since in the experiments there is no rigid plane limiting the ambient fluid, a space gradient/inclination of the free surface (between ambient fluid and air) appears in order to accelerate the ambient fluid toward the sink. Furthermore, the theoretical sink is distributed over the contact area of the ambient with the side-wall, while the real sink is rather a concentrated outflow. These differences between the ideal and real boundary conditions must be taken into consideration in the assessment of the validity of the theoretical model. Since the crest level of the weir at the sink end of the channel is fixed, an increment of H^* is expected, which in turn modifies all the balances of the present model. In order to evaluate this increment, some experiments were performed measuring the free surface displacement with Ultrasonic distance meters.

Figure 11 shows the level displacement as a function of the front position measured by four Ultrasonic distance meters, and shown vis-a-vis the front speed and inflow and outflow rates. The gray thick curve is the theoretical uniform free surface displacement obtained by integrating the mass conservation equation:

$$\frac{d\mathcal{V}}{dt} = Q_{in} - Q_{out}, \tag{13}$$

where $\mathcal{V} = \mathcal{V}(h(t))$, $Q_{in}(t)$ is the inflow rate (of the dense fluid current) and $Q_{out}(t)$ is the outflow rate (of the ambient fluid). Although mixing occurs in the experiments, eq. (13) assumes the two fluids are separated by a sharp interface without mixing. The outflow rate was estimated by calibrating the weir with respect to the free surface level measured by the sensor Us4, positioned 10 cm upstream with respect to the crest.

After starting the fluid injection, the front of the current accelerates, reaches a maximum speed corresponding to the peak of the inflow rate at $x_N \approx 12$. In this phase the outflow rate is still null and the displaced ambient fluid is stored in the channel, with a vertical positive displacement of the open interface; the deceleration/acceleration is modulated by the local average pressure gradient of the ambient fluid shown in the mid panel, which is computed by considering the free surface vertical displacement measured by the nearest distance meters: e.g., for $x_{Us1} < x_N < x_{Us2}$ results $i = -(\Delta H_{Us2} - \Delta H_{Us1})/(x_{Us2} - x_{Us1})$, for $x_{Us2} < x_N < x_{Us3}$ results $i = -(\Delta H_{Us3} - \Delta H_{Us2})/(x_{Us3} - x_{Us2})$. For $x_N > x_{Us3}$ an almost uniform flow condition is reached, even though a small imbalance in the discharges is still present (see the upper panel), and the average free-surface gradient is com-

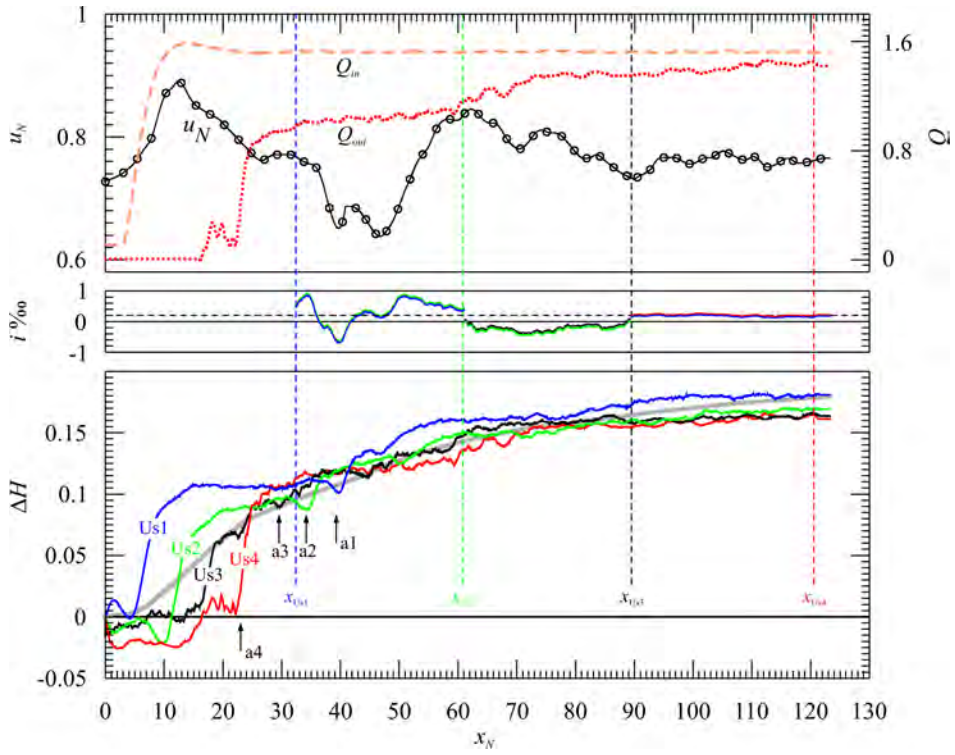

Figure 11: Experiment #58. The lower panel shows the non dimensional level displacement ΔH measured by the four Ultrasonic distance meters (blue, green, black, and red curves). The gray thick curve in the lower panel is the theoretical free surface level displacement. The mid panel shows the average free surface spatial gradient, $i = -\partial H/\partial x$, and the upper panel shows the front speed u_N and the inflow and the outflow rates, Q_{in} and Q_{out}, respectively. The arrows $a_1 - a_4$ indicate the negative surges generated by the reflection of the positive surges at the exit section.

puted considering Us1 and Us4 as $i = -(\Delta H_{Us4} - \Delta H_{Us1})/(x_{Us4} - x_{Us1})$. The dashed horizontal line in the mid panel is the free-surface gradient needed to balance the energy losses of the ambient fluid (with opposite sign, since $i = -\partial h/\partial x$). The gradient is theoretically equal to $\approx$ 0.02%; any difference with respect to this reference value is available for acceleration/deceleration of the fluid. This observation applies also to the intruding current of denser fluid, showing that at different locations along the channel the front of the intruding current accelerates or decelerates.

Some free surface disturbances travel toward the exit section and then, after reflection, travel back (see the arrows with symbol 'a' in Figure 11). The first negative surge appears in section x_{Us4} when the front is at $x_N \approx 25$ and travels back as a kinematic wave with a velocity equal to $\sqrt{gH_m^*} - u_N(1-\varphi)$, where H_m^* is the mean ambient fluid depth $H_m^* = A_a/W$, $A_a \equiv A_T$ and W is the width of the ambient fluid current at the interface with air.

4.2. The velocity profiles

In order to enhance the understanding of the overall dynamics of the intruding current and of the ambient fluid, for some experiments the profile of the horizontal velocity was acquired by an Ultrasonic Velocity Profiler (DOP 2000, Signal Processing, Switzerland). The probe of the instrument emits bursts of Ultrasounds at a frequency (carrier) of 8 MHz and then receives the echoes generated by the reflection of seeding particles or turbulence eddies (targets) moving in the current. The echoes have a Doppler shift proportional to the velocity of the particles with respect to the axis of the probe. The position of the targets can be measured by knowing the celerity c of the Ultrasounds in the fluid along the path from the emitter/receiver and the targets, and the time lag Δt between emission and return of the echoes is equal to $x = c\Delta t/2$ for a homogeneous fluid; the celerity of the Ultrasounds ($\approx$ 1500 $\mathrm{m\,s^{-1}}$) depends on mass density and compressibility of the fluid. However, since in the present experiments the path of the Ultrasounds is partly in the ambient fluid and partly in the denser fluid of the intruding current, the position of the targets should be computed as $2\int_0^x dx'/c(x') = \Delta t$, being $c(x')$ the US celerity at the position x' along the path, which is also subject to refraction. The celerity $c(x')$ was known only in the ambient fluid and in the denser current, but it was unknown in the intermediate layer. An approximate scaling of the targets position was performed by imposing that the echo of the tank wall was located at the correct distance

from the emitter/receiver and that the spike of energy corresponding to the approximate interface was at the observed position of the interface.

The size of the volume of measurement in the axial direction depends on the number of cycles per burst, whereas in the transverse direction it depends on the geometry of the emitter and on the frequency of the carrier: in the used probe the Ultrasounds propagate diverging with a 1.2° half angle, with an emitter (the active element) of 0.5-cm diameter. At the maximum distance of 10 cm, the volume of measurement is a cylinder with diameter of $\approx$ 0.9 cm and coaxial to the probe. The velocity is computed by elaborating the frequency (Doppler) shift and averaging several bursts per profile (8 bursts per profile in the present experiments), with a resolution of 1/128 of the velocity range. Considering all the sources of uncertainties, the overall accuracy of velocity measurements is better than 4 % of the instantaneous value, with a minimum of 0.3 cm/s. The overall accuracy of the measurements is also based on the hypothesis that the velocity of the intruding current is parallel to the bottom (see Appendix C). The measured velocity is affected by fluid velocity components in the vertical direction, which are expected in particular at the interface between the ambient fluid and the intruding current and during the head passage where instabilities generate billows. Measurements in the body of the current are much less contaminated and the error is minimum near the walls. The quantitative estimation of the uncertainty related to the mentioned 3D phenomena would have required a set of two or three probes at the same section of measurement as reported in [17], but this was beyond the purposes of the present work.

A key element of the velocity measurements in the present experiments is the absence of seeding particles in the ambient fluid, whereas the intruding current fluid does not require seeding since the eddies and the fluctuation of density are quite effective in reflecting the echoes of the UVP [see, e.g., 19, 20]. As a result, the measured velocity profiles refer only to the intruding current and not to the ambient fluid, except for the later stage, when part of the denser fluid is mixed with the ambient fluid and acts as a tracer for the UVP measurements. However, the measured profiles should be considered with cautions, since no specific experimental activity has been devoted to check the efficiency of density fluctuations as tracers in this kind of (complex) flows.

Figures 12-13 show the velocity profiles for two experiments with similar parameters but a different value of γ. The standard deviation of the velocity is also shown; it is proportional to the (macro)turbulence intensity, but also

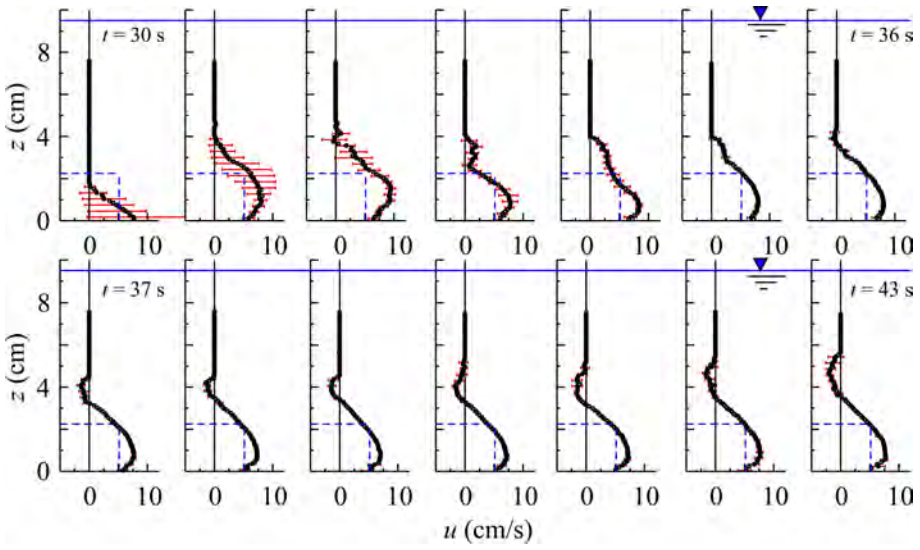

Figure 12: Velocity profiles measured at $x = 165\,\mathrm{cm}$ for Exp. #16, $\gamma = 1$ (outflow and inflow section at the same end of the channel). The horizontal bars (red online; one out of three is plotted for clarity) indicate the standard deviation of the measured velocity and are proportional to the turbulence level. The dashed horizontal lines indicate the depth of a current advancing with a uniform velocity equal to the measured front speed, represented by the vertical dashed line. The time step between two frames is 1 s, each profile is the average of 1 s of acquisition (44 profiles).

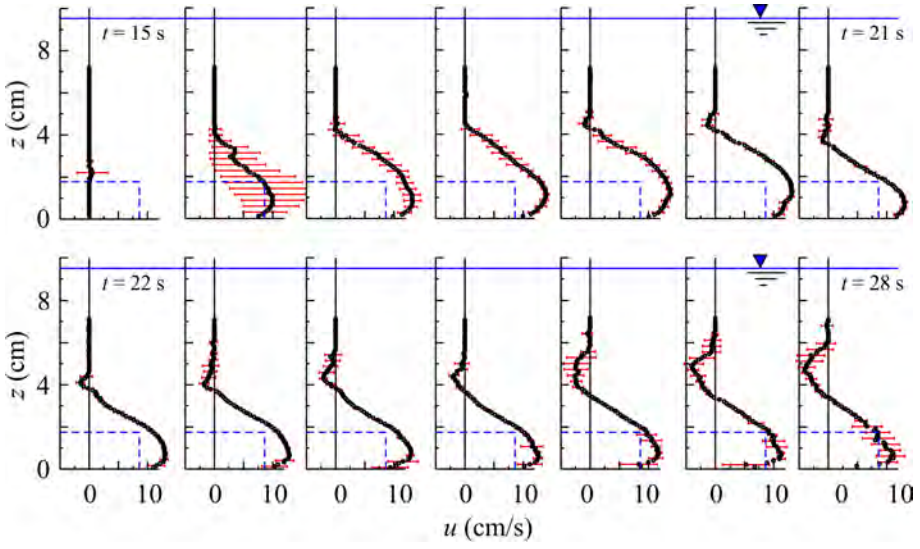

Figure 13: Velocity profiles for Exp. #34, $\gamma = 0$ (outflow section at the opposite end of the channel with respect to inflow section). For caption see Figure 12.

connected to the entrainment of ambient fluid at the interface and at the nose of the current. The maximum velocity of the current is larger than the front speed, equal to 5.3 cm/s for Exp. #16, and to 8.6 cm/s for Exp. #34, respectively, and it requires a strong returning flow in the horizontal plane and in the vertical to fulfill mass conservation. For the return flow case (Exp. #16, $\gamma = 1$) the mixing between the two fluids is apparently enhanced, but the opposite flow of the ambient fluid confines the intruding current. The turbulence level is generally higher at the arrival of the nose, then it reduces; its maximum value is reached near the interface and near the bottom. A return flow of the ambient fluid is also observed. This is due to a partial mixing between the ambient fluid and the denser fluid, with the latter acting as a tracer of the flow field of the former. In Appendix C the results of an additional experiment in condition identical to Experiment #34 are shown, but measuring the fluid velocity with two UVP probes, obtaining the horizontal and the vertical velocity. The vertical velocity is generally much smaller than the horizontal velocity, with some fluctuations in the mixing area.

We recall that the SW theory assumes z-independent u, with a sharp discontinuity at the interface. The measured velocity profiles are far from uniform and display a rather smooth transition about the interface. The latter can be attributed to three dimensional effects with billows.

5. Conclusions

We have analysed the propagation of a GC released in a horizontal channel of circular cross-section for constant and time varying inflow. The theoretical model has been compared with two series of experiments, 45 conducted with constant inflow and 15 with time varying inflow. The dense fluid was a saline solution injected by a pump controlled via software, the ambient fluid was tap water. The time series of front position was measured for all tests, the levels of the open air-water interface and the velocity profiles of the intruding current were measured for a subset of tests. The novelties of the present investigation are: (i) the circular shape of the cross-section of the channel, to the best of our knowledge adopted for the first time to test the propagation of constant or time varying flux GC; (ii) the verification of the effects of the ambient fluid flow and the analysis of their dependence on the position of the outflow section; (iii) the experimental verification of the choking effect, corresponding to the theoretical limit of energetically admissible

GC propagation; (iv) the description of the effects of the open interface.

The front speed as predicted by the theoretical model is in good agreement with the experiments, in particular for the return flow case. As concerning the predicted choking behavior, the experimental support is not sharp. In general we observed a qualitative change (reduced influence of influx conditions) when Q approaches or exceeds the theoretical Q_{chok}, but a clear-cut plateau of u_N vs. Q was attained only for return-flow systems. The agreement is less good for the no-return flow experiments, with theory systematically over-predicting the experimental front speed. The Reynolds number is sufficiently large to guarantee that viscous effects, although present, play a marginal role in the current dynamics (the Reynolds number based on the ambient fluid height and on the velocity scale is $> 4.5 \times 10^3$, the Reynolds number based on the intruding current height and velocity is $> 10^3$). More significant contributors to the discrepancy are the effects of the open interface and the velocity distribution. The flow of the ambient fluid displaced by the intruding currents determines an increment of the level of the air-water interface and a free-surface (i.e. pressure) gradient which, in turn, accelerates/decelerates the intruding current, favoring billows and enhancing three dimensional effects. The increment of the free-surface level is of the order of several millimetres compared to a maximum depth of the ambient fluid equal to 95 mm ($\beta = 1$), with a significant variation (ranging from -2.5 to 18%) of the parameters β and H^* with respect to the nominal (initial) values. Some measurements of the intruding current velocity taken at a section far from the entrance (in that section the influence of the geometry of the inflow is lost) show that the velocity profile is not uniform. Observing the shape of the measured velocity profile, we can conclude that recirculation occurs in both vertical and horizontal plane.

In order to substantiate the hypotheses on the source of discrepancies, a refinement of the inviscid GC model should include dissipative effects near the nose of the intruding current, non uniform velocity profiles, and dissipations in the body of the current. A numerical model based on the method of characteristics, following [21] is expected to provide the platform for the improved model. Navier-Stokes simulations could exclude entirely the friction at the bottom and fluctuations at the top, and a further validation of the model shall require experiments with an outflow at both end sections of the channel (γ between 0 and 1), and different cross-sectional shapes. Another issue that requires attention is entrainment/mixing. According to [22] this effect is influential only after a very long distance of propagation, but nev-

ertheless an in-depth analysis is expected to enhance the understanding of the flow field (see, e.g., [23, 24] and the references therein). In this context, we emphasize that almost all available studies on mixing are concerned with rectangular lock-release GCs, and the applicability of that insights to our very different GC flow is questionable. These tasks require a good deal of additional time and resources, and are left for future work.

Acknowledgements

We are grateful to the editor and the reviewers for their comments, which improved the quality of the manuscript.

Appendices

A. Viscous-buoyancy balance

The viscous forces can be computed according to the model developed in [25] upon considering a Newtonian fluid. For $h < r^*$ (this condition is usually satisfied by our system) the circular cross section can be approximated by a parabola and the viscous forces on the body of the current are equal to (dimensional values)

$$F_V = \frac{4\sqrt{2}}{3K_c}\rho_c\nu_c\frac{u_N}{h_N^2}A(h_N)x_N, \tag{A.1}$$

where $K_c = 0.43$ and where we have neglected the interaction with the ambient fluid, while the buoyancy forces are

$$F_B = \rho_a g' \int_0^{h_N} (h_N - z)f(z)dz = \rho_a g'[A(h_N)h_N - J(h_N)]. \tag{A.2}$$

We are using a box-model approximation with a constant thickness of the current, i.e., $h(t) = h_N(t)$ independent of the space variable x. For $F_V = F_B$ eqs. (A.1) and (A.2) yield

$$u_N = \frac{3K_c}{4\sqrt{2}}\frac{g'}{R\nu_c}h_N^2\left(h_N - \frac{J}{A}\right)\frac{1}{x_N}, \quad \text{with } R \approx 1, \tag{A.3}$$

and, in dimensionless form

$$u_N = \frac{3K_c}{4\sqrt{2}} Re h_N^2 \left(h_N - \frac{J}{A} \right) \frac{1}{x_N}. \tag{A.4}$$

Approximating the circular cross-section by a parabola of equation $z = y^2/(2r)$, the area is $A = 4/3(2/\beta h_N^3)^{1/2}$ and $J = 4/5(2/\beta h_N^5)^{1/2}$ ($A = 4/3(2rh_N^3)^{1/2}$ and $J = 4/5(2rh_N^5)^{1/2}$ are the dimensional counterparts, respectively). Substituting the expression of A and J (in dimensionless variables) of the approximate cross-section, eq. (A.4) becomes

$$u_N = \frac{3K_c}{10\sqrt{2}} Re \frac{h_N^3}{x_N}, \text{ with } \frac{3K_c}{10\sqrt{2}} \approx 0.09. \tag{A.5}$$

Assuming the following simplified behavior (dimensionless variables)

$$\begin{cases} x_N = Kt^\delta, \\ u_N = \delta K t^{\delta-1}, \\ \mathcal{V}(t) = qt^\alpha, \\ A(h_N) = \dfrac{\mathcal{V}(t)}{x_N} \rightarrow h_N = \left[\dfrac{3}{4} \sqrt{\dfrac{\beta}{2}} \dfrac{q}{K} \right]^{2/3} t^{2(\alpha-\delta)/3}, \end{cases} \tag{A.6}$$

by equating the powers of t and the coefficients in eq. (A.5) it results

$$\delta_V = \frac{2\alpha+1}{4}, \quad K_V = \sqrt{q} \left(\frac{27}{80\sqrt{2}} \right)^{1/4} \left(\frac{Re\beta K_c}{2\alpha+1} \right)^{1/4}, \tag{A.7}$$

where the subscript V indicates the dominance of viscous (laminar) effects.

Let us consider the viscous non-laminar regime. In general, the tangential stress of the current at the wall can be expressed as

$$\tau_w = \rho_c \frac{\lambda}{8} u^2, \tag{A.8}$$

where λ is the Darcy friction factor. Assuming Blasius' expression [26] for the friction factor in turbulent regime for smooth walls

$$\lambda = 0.3164 Re_c^{-1/4}, \; Re_c = \frac{4u(A/B)}{\nu_c}, \; 4000 < Re_c < 10^5, \tag{A.9}$$

where $B(h)$ is the 'wet perimeter' (the perimeter of the cross section of the current in contact with the wall), the drag in turbulent regime is

$$F_{VT} = k_t \rho_c \nu_c^{1/4} B(h_N) \left(\frac{B(h_N)}{A(h_N)} \right)^{1/4} u_N^{7/4} x_N, \; k_t = \frac{0.3164}{8(4)^{1/4}}. \tag{A.10}$$

The Reynolds number of the current, Re_c, can be expressed in terms of the Reynolds number Re of the ambient fluid as

$$Re_c = 4 u_N \frac{A}{B} Re, \tag{A.11}$$

where the remaining variables are dimensionless.

For $F_{VT} = F_B$ eqs. (A.10) and (A.2) yield

$$u_N = \frac{1}{k_t^{4/7}} \frac{g'^{4/7}}{R^{4/7} \nu_c^{1/7}} \frac{A^{5/7}}{B^{5/7}} \left(h_N - \frac{J}{A} \right)^{4/7} \frac{1}{x_N^{4/7}}, \text{ with } \frac{1}{k_t^{4/7}} \approx 0.13, \; R \approx 1, \tag{A.12}$$

and, in dimensionless variables

$$u_N = \frac{Re^{1/7}}{k_t^{4/7}} \frac{A^{5/7}}{B^{5/7}} \left(h_N - \frac{J}{A} \right)^{4/7} \frac{1}{x_N^{4/7}}. \tag{A.13}$$

Introducing in eq. (A.13) the expressions for A and J as computed for the parabola approximating the circular cross-section, and expressing the wet perimeter as $B \approx 2(2h_N/\beta)^{1/2}$ ($B \approx 2(2rh_N)^{1/2}$ is its dimensional counterpart), yields

$$u_N = \frac{1}{k_t^{4/7}} \left(\frac{2}{3} \right)^{5/7} \left(\frac{2}{5} \right)^{4/7} Re^{1/7} \frac{h_N^{9/7}}{x_N^{4/7}}, \text{ with } \frac{1}{k_t^{4/7}} \left(\frac{2}{3} \right)^{5/7} \left(\frac{2}{5} \right)^{4/7} \approx 0.057. \tag{A.14}$$

Introducing the expressions for x_N, u_N and h_N of the simplified model (A.6) in eq. (A.14) and equating the exponents of t and the coefficients results in the expression

$$\delta_{VT} = \frac{6\alpha + 7}{17}, \quad K_{VT} = \left(\frac{3}{2^6 5^4} \right)^{1/17} \left(\frac{q^6 Re \beta^3}{k_t^4} \right)^{1/17} \left(\frac{17}{6\alpha + 17} \right)^{7/17}, \tag{A.15}$$

where the subscript VT indicates that the flow is dominated by viscous turbulent effects. If we assume that the current is in fully developed turbulent

regime, λ is constant for a given relative roughness of the wall, and balancing again the drag and the buoyancy forces, results

$$u_N = \left(\frac{8g'}{\lambda}\right)^{1/2} \left(\frac{A}{B}\right)^{1/2} \left(h_N - \frac{J}{A}\right)^{1/2} \frac{1}{x_N^{1/2}}, \tag{A.16}$$

and, in dimensionless variables

$$u_N = \left(\frac{8}{\lambda}\right)^{1/2} \left(\frac{A}{B}\right)^{1/2} \left(h_N - \frac{J}{A}\right)^{1/2} \frac{1}{x_N^{1/2}}. \tag{A.17}$$

With the usual approximations for A, B and J, eq. (A.17) becomes

$$u_N = \left(\frac{32}{15\lambda}\right)^{1/2} \frac{h_N}{x_N^{1/2}}, \tag{A.18}$$

which, upon substituting the expressions of the simplified model (A.6), yields

$$\delta_{FT} = \frac{4\alpha + 6}{13}, \quad K_{FT} = \left(\frac{3(2)^5}{5^3}\right)^{1/13} \left(\frac{q^4\beta^2}{\lambda^3}\right)^{1/13} \left(\frac{13}{4\alpha + 6}\right)^{6/13}. \tag{A.19}$$

Figure 14 depicts the behavior of the time exponents for the three cases of current in viscous laminar regime, in viscous turbulent regime and in fully turbulent regime, with $\delta_{VT} > \delta_V$ if $\alpha < 11/10$ and $\delta_{FT} > \delta_{VT}$ if $\alpha < 11/10$.

B. Inertial-viscous balance

We use a box-model approximation, assuming that the current is thin so that Fr is a constant and the flow in the ambient fluid is negligible. By conjecturing that the nose condition (2) is still governing the propagation of the current in time varying inflow, substituting the expression for u_N and for h_N into (A.6) and equating the exponent of the time and the coefficients, results

$$\delta_I = \frac{\alpha + 3}{4}, \quad K_I = \left(\frac{4Fr}{\alpha + 3}\right)^{3/4} \left(\frac{3}{4}\sqrt{\frac{\beta}{2}}\right)^{1/4}, \tag{B.1}$$

where the subscript I indicates that the flow is dominated by inertia (for a rectangular section $\delta_I = (\alpha + 2)/3$).

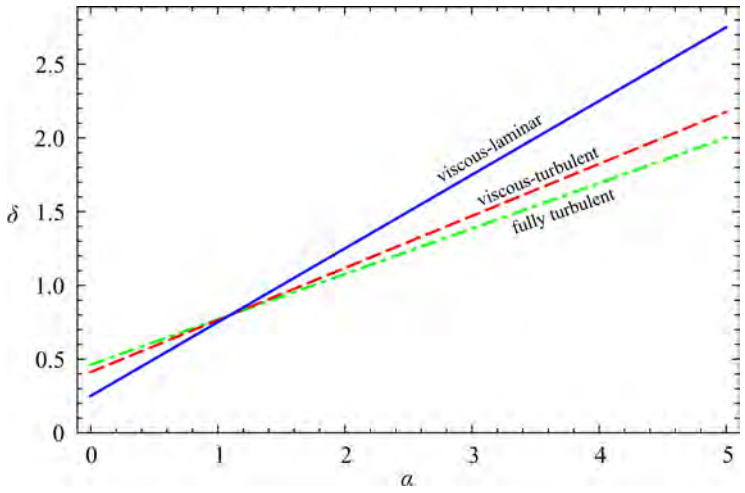

Figure 14: The power δ as a function of α for the viscous-laminar, the viscous-turbulent and the fully turbulent regimes of a current in a circular cross-section.

The inertial forces are

$$F_I = \rho_c \int_0^{x_N} u u_x A(h_N) dx = \frac{1}{2} \rho_c u_N^2 A(h_N). \tag{B.2}$$

The ratio with the viscous forces in eq. (A.1) yields

$$\frac{F_I}{F_V} = \frac{3K_c}{8\sqrt{2}} \frac{u_N}{\nu_c} \frac{h_N^2}{x_N}, \tag{B.3}$$

or, in dimensionless form

$$\frac{F_I}{F_V} = \frac{3K_c}{8\sqrt{2}} Re\, u_N \frac{h_N^2}{x_N}. \tag{B.4}$$

Substituting the expression for u_N, x_N and h_N of the simplified model (A.6) yields

$$\frac{F_I}{F_V} = \frac{3K_c}{8\sqrt{2}} Re\, \delta_I \left(\frac{3}{4} \sqrt{\frac{\beta}{2}} \frac{q}{K_I} \right)^{4/3} t^{(4\alpha - 7\delta_I)/3}, \tag{B.5}$$

and introducing the expression of the time $t = (x_N/K)^{1/\delta}$ gives

$$\frac{F_I}{F_V} = \frac{3K_c}{8\sqrt{2}} Re\, \delta_I \left(\frac{3}{4} \sqrt{\frac{\beta}{2}} \frac{q}{K_I} \right)^{4/3} \left(\frac{x_N}{K_I} \right)^{(10\alpha - 21)/(2\alpha + 9)}, \tag{B.6}$$

which, for $\alpha = 1$, reduces to $F_I/F_V \propto x_N^{-1}$.

C. Measuring the vertical velocity of the intruding current

In order to estimate the effects of the vertical velocity in a single UVP probe measurements, we have repeated Exp. #34 installing two probes, one of them orthogonal to the bottom and the second at an angle of 75° with respect to the horizontal, both in a vertical plane through the axis of the pipe. The two probes are used in multiplexing, by acquiring alternatively a velocity profile from probe 1 and probe 2, with data having a negligible time delay. The two velocity components in a $x - z$ coordinate system are given by

$$u = (u_2 - u_1 \cos\theta)/\sin\theta \tag{C.1}$$

$$v = -u_1, \tag{C.2}$$

v is the vertical velocity positive upward and u_1 and u_2 are the velocities measured by the two probes along their axes. Figure 15*ab* shows the layout and Figure 15*c* shows the velocity profiles. The vertical velocity component is much smaller than the horizontal velocity, with larger fluctuations in a region near the interface. The horizontal velocity profiles are similar to those obtained with a single probe and shown in Figure 13. The average difference between the horizontal velocity measured with a single probe and two probes is 8.5% with a peak value of 17.2%. These values must be compared with the uncertainty due to the characteristics of the instrument and to the geometry. With a single probe configuration the uncertainty on the horizontal velocity u is due to the intrinsic uncertainty of the instrument (relative value equal to 4%), to the angle of the probe (absolute error of the digital level equal to 0.1°), and to the space variability of the flow field (which depends on the flow characteristics). With two probes the uncertainty increases since u is a function of u_1, u_2, θ_1 and θ_2, where θ_1 and θ_2 are the angles of the two probes ($\theta_1 = 0$ and $\theta_2 = 15°$ in the adopted configuration). In addition, only some of the volumes of measurement of the two probes overlap and the space variability of the flow field has a larger impact on the uncertainty than for a single-probe measurement. In conclusion, the overall uncertainty is strictly related to the characteristics of the single experiment, but for GCs characterised by a dominant horizontal dynamics a single UVP probe gives results with an uncertainty (due to the measurement errors and to the

presence of a vertical velocity) comparable to the uncertainty obtained in a two-probe configuration.

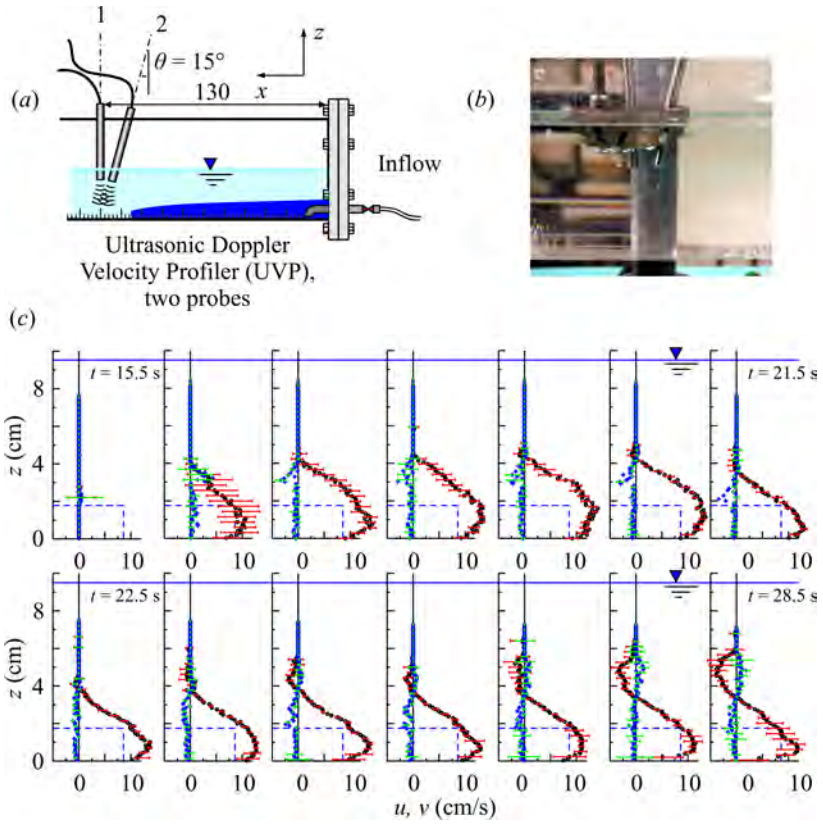

Figure 15: (a) Layout of the two UVP probes, and (b) a photograph of the two probes during testing; (c) horizontal (circles) and vertical (pluses) velocity profiles measured at $x = 130$ cm for an experiment reproducing the conditions of Exp. #34, $\gamma = 0$ (outflow section at the opposite end of the channel with respect to inflow section). The horizontal bars (red and green online; one out of three is plotted for clarity) indicate the standard deviation of the measured velocity and are proportional to the turbulence level. The dashed horizontal lines indicate the depth of a current advancing with a uniform velocity equal to the measured front speed, represented by the vertical dashed line. The time step between two frames is 1 s, each profile is the average of 1 s of acquisition (44 profiles).

References

[1] J. E. Simpson, Gravity Currents in the Environment and the Laboratory, Cambridge University Press, 1997.

[2] M. Ungarish, An Introduction to Gravity Currents and Intrusions, CRC Press, 2009.

[3] S. Longo, M. Ungarish, V. Di Federico, L. Chiapponi, A. Maranzoni, The propagation of gravity currents in a circular cross-section channel: experiments and theory, J. Fluid Mech. 764 (2015) 513–537.

[4] J. Monaghan, C. Mériaux, H. Huppert, J. Monaghan, High Reynolds number gravity currents along v-shaped valleys, European Journal of Mechanics - B/Fluids 28 (5) (2009) 651–659.

[5] A. Cuthbertson, P. Lundberg, P. Davies, J. Laanearu, Gravity currents in rotating, wedge-shaped, adverse channels, Environmental Fluid Mechanics 14 (5) (2014) 1251–1273. doi:10.1007/s10652-013-9285-4.

[6] C. S. Jones, C. Cenedese, E. P. Chassignet, P. F. Linden, B. R. Sutherland, Gravity current propagation up a valley, Journal of Fluid Mechanics 762 (2015) 417–434. doi:10.1017/jfm.2014.627.

[7] C. Kranenburg, Gravity-Current front advancing into horizontal ambient flow, J.Hydraul. Eng. 119 (1993) 369–379.

[8] C. Kranenburg, Unsteady gravity currents advancing along a horizontal surface, J.Hydraul.Res. 31(1) (1993) 49–60.

[9] J. Bühler, S. J. Wright, Y. Kim, Gravity currents advancing into a coflowing fluid, J. Hydraul. Res. 29 (1991) 243–257.

[10] M. Shringarpure, H. Lee, M. Ungarish, S. Balachandar, Front conditions of high-re gravity currents produced by constant and time-dependent influx: An analytical and numerical study, European Journal of Mechanics - B/Fluids 41 (0) (2013) 109 – 122. doi:http://dx.doi.org/10.1016/j.euromechflu.2013.04.004.

[11] T. Maxworthy, Gravity currents with variable inflow, J. Fluid Mech. 128 (1983) 247–257.

[12] A. J. Hogg, M. A. Hallworth, H. E. Huppert, On gravity currents driven by constant fluxes of saline and particle-laden fluid in the presence of a uniform flow, J. Fluid Mech. 539 (2005) 349–385. doi:10.1017/S002211200500546X.

[13] M. A. Hallworth, A. J. Hogg, H. E. Huppert, Effects of external flow on compositional and particle gravity currents, J. Fluid Mech. 359 (1998) 109–142. doi:10.1017/S0022112097008409.

[14] T. B. Benjamin, Gravity currents and related phenomena, J. Fluid Mech. 31 (1968) 209–248.

[15] M. Ungarish, A general solution of Benjamin-type gravity current in a channel of non-rectangular cross- section, Environ Fluid Mech 12 (3) (2012) 251–263.

[16] M. Ungarish, Two-layer shallow-water dam-break solutions for gravity currents in non-rectangular cross-area channels, J. Fluid Mech. 732 (2013) 537–570.

[17] S. Longo, Experiments on turbulence beneath a free surface in a stationary field generated by a crump weir: free-surface characteristics and the relevant scales, Experiments in Fluids 49 (6) (2010) 1325–1338. doi:10.1007/s00348-010-0881-5.

[18] S. Longo, Experiments on turbulence beneath a free surface in a stationary field generated by a crump weir: turbulence structure and correlation with the free surface, Experiments in Fluids 50 (1) (2011) 201–215. doi:10.1007/s00348-010-0921-1.

[19] Y. Takeda, Ultrasonic Doppler Velocity Profiler for Fluid Flow, Vol. 101 of Fluid Mechanics And Its Applications, Springer Netherlands, 2012. doi:10.1007/978-4-431-54026-7.

[20] S. Eckert, A. Cramer, G. Gerbeth, Velocity measurement techniques for liquid metal flows, in: Magnetohydrodynamics, Vol. 80 of Fluid Mechanics And Its Applications, Springer Netherlands, 2007, pp. 275–294. doi:10.1007/978-1-4020-4833-3-17.

[21] M. Ungarish, Shallow-water solutions for gravity currents in non-rectangular cross-area channels with stratified ambient, Environmental Fluid Mechanics (2015) 1–28doi:10.1007/s10652-014-9383-y.

[22] C. G. Johnson, A. Hogg, Entraining gravity currents, Journal of Fluid Mechanics 731 (2013) 477–508. doi:10.1017/jfm.2013.329.

[23] A. T. Fragoso, M. D. Patterson, J. S. Wettlaufer, Mixing in gravity currents, Journal of Fluid Mechanics 734. doi:10.1017/jfm.2013.475.

[24] C. Adduce, G. Sciortino, S. Proietti, Gravity currents produced by lock exchanges: Experiments and simulations with a two-layer shallow-water model with entrainment, Journal of Hydraulic Engineering 138(2) (2012) 111–121.

[25] S. Longo, V. Di Federico, L. Chiapponi, Non-newtonian power-law gravity currents propagating in confining boundaries, Environmental Fluid Mechanics 15 (2015) 515–535. doi:10.1007/s10652-014-9369-9.

[26] H. Blasius, Das aehnlichkeitsgesetz bei reibungsvorgngen in flssigkeiten, Mitteilungen ber Forschungsarbeiten auf dem Gebiete des Ingenieurwesens 131.